Particles II

Access the latest eBook →

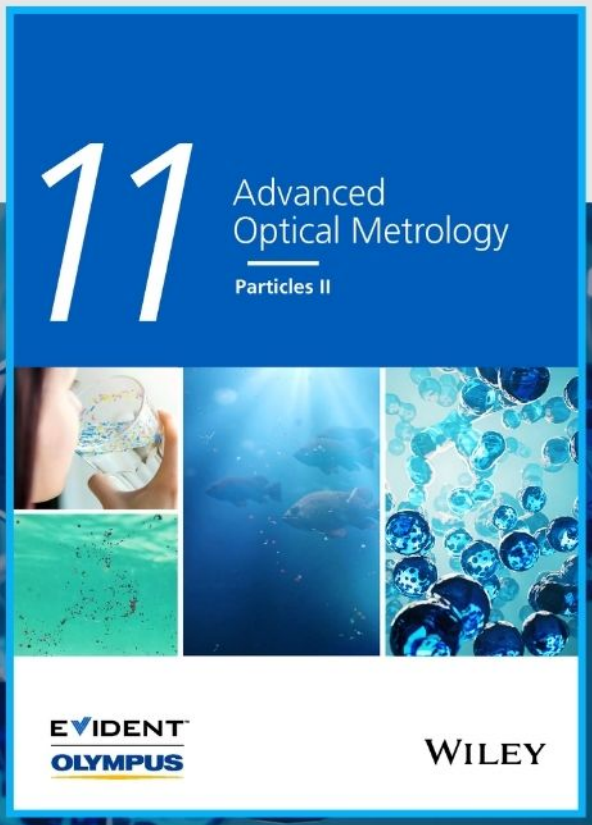

Impact on Biological Systems and the Environment

This eBook is dedicated to the research of Professor David Wertheim.
In collaboration with various groups, Professor Wertheim uses confocal microscopy to analyse the impact of different types of particles on human health and the environment, with a focus on human health-hazardous particles detected with solid-state nuclear track detectors (SSNTD). Download for free, today.

EVIDENT
OLYMPUS

WILEY

ADVANCED FUNCTIONAL MATERIALS
www.afm-journal.de

Magnetostrictive and Electroconductive Stress-Sensitive Functional Spider Silk

Federico Spizzo, Gabriele Greco,* Lucia Del Bianco, Marco Coïsson, and Nicola M. Pugno**

Electronics and soft robotics demand the development of a new generation of hybrid materials featuring novel properties. Among these, remarkable mechanical properties are required to sustain mechanical stresses, and electrical and magnetic properties are essential to design the devices' interface. In this work, a hybrid material is presented, consisting of a spider silk thread, providing mechanical robustness, coated with a layer of a magnetostrictive FeCo alloy, which ensures both electrical conductivity and stress-sensitive magnetic properties. The durability and the homogeneity of the composite are validated, as well as its ability to respond to magnetic and mechanical stimuli. Despite the coating, the soft nature of the silk and its mechanical performances are preserved. The magnetic study reveals that the magnetic behavior of the film is strongly affected by the silk thread–FeCo layer interaction, especially under mechanical stresses. Indeed, when the composite is subjected to tensile strain, the magnetic signal changes accordingly, indicating that the layer–silk interaction is maintained and can be exploited to reveal the tensional state of the sample even under severe cycles. Therefore, the presented hybrid material is a flexible fiber with properties that are suitable for magneto-electronics applications, e.g., magnetic actuators as well as strain/stress sensors.

1. Introduction

The development of flexible materials with magnetic and electronic properties has raised in these decades the interest of scientists due to their technological potential.[1,2] The aim of these materials is to provide integrated solutions that offer both electrical and magnetic properties combined with stretchability, compressibility, twistability, bendability, and in general deformability.

Common electronics and magnetic materials, such as silicon or ferromagnetic alloys, are rigid and fragile. On the contrary, many biological materials are soft, elastic, and offer inspiration to design structural materials with desired properties.[3,4] For example, artificial skin that resembles the natural counterpart may be used in soft robotics, provided its mechanical similarity with respect to the natural skin.[5,6] Artificial skin also provides a roadway toward wearable sensing devices, which enables a natural interaction between the body and the device itself, allowing people to have a personalized healthcare.[7] Moreover, these devices are stretchable and possibly fatigue free while performing their monitoring functions that integrate physical and chemical features on the same wearable platform.[8] Thus, the aimed flexible electronics devices must sustain repeated bending and stretching as well as have the possibility to perform multiple functions. Furthermore, to reduce the impact of the electronics contacts, the components of the electronic devices must be micrometric in size (wires of ≈2–10 µm in diameter)[9] and lightweight.[10] In this context, magnetic actuation fibers (e.g., amorphous magnetic microwires[11]) play a crucial role in soft robotics, since they combine the high tensile strength with the high compliance and desired functionality.[12] Magnetic actuation fibers can be produced in several ways:[12] coating fibers with water based solutions,[13] electrospinning,[14] and 3D printing of the magnetic microparticles–polymers composites.[12]

To expand such frontiers, silk represents a good basic material for such soft components, since its properties align with the ones of many soft tissues, and thus it allows scientists to achieve a smaller mismatch in mechanical properties between electronics component and the working environment.[1,9,15] In terms of mechanical properties, silk can be used in a composite to provide compliance and stretchability as well as strength to weak materials.[16] However, having a poor conductivity, silks need to

F. Spizzo, L. Del Bianco
Department of Physics and Earth Science
University of Ferrara and INFN - Sezione di Ferrara
via G. Saragat, 1, Ferrara I-44122, Italy
E-mail: federico.spizzo@unife.it
G. Greco, N. M. Pugno
Laboratory for Bioinspired, Bionic, Nano, Meta, Materials & Mechanics
Department of Civil
Environmental and Mechanical Engineering
University of Trento
Via Mesiano, 77, Trento I-38123, Italy
E-mail: gabriele.greco-2@unitn.it; nicola.pugno@unitn.it
M. Coïsson
Nanoscience and Materials Division
INRIM
Str. delle Cacce, 91, Torino I-10135, Italy
N. M. Pugno
School of Engineering and Materials Science
Queen Mary University of London
Mile End Road, London E1 4NS, UK
The ORCID identification number(s) for the author(s) of this article can be found under https://doi.org/10.1002/adfm.202207382.

DOI: 10.1002/adfm.202207382

be hybridized with materials that can convey such property. In this context, silkworm silk has been used to produce electrical devices, such as electronic skin for medical applications.[17] Unfortunately, despite the acceptable conductivity, many silkworm silk based devices present poor mechanical properties,[18,19] which can be overcome by using spider silk instead. In fact, although silks are produced by several arthropods, the spider ones have been studied since a long time[20,21] because of their superior mechanical and biological properties with respect to the silkworms.[22–26]

Therefore, spider silk was hybridized to produce a magnetic composite by using a water dispersion of magnetic particles.[27] However, due to the exposure to water that irreversibly plasticizes spider silks,[28,29] the produced material presented reduced mechanical properties.[26,30] Unfortunately, no magnetic as well as electric characterization was available.

To hybridize spider silks with metals, the exposure of the fibers to vapors doped with heavy metals seemed to improve the mechanical properties.[31] However, also in this case no electronic and magnetic characterizations were performed. In this regard, the deposition of evaporated gold on spider silk provides electrical conductivity, which resists if the composite works with deformations below the yielding point.[32]

Spider silk may be also hybridized with nanomaterials, such as graphene[33] or carbon nanotubes[34,35]. Spider silk bundles have been combined with carbon nanotubes by means of a water dispersion.[34] Despite the decrease in strength due to water, the silk presented still acceptable mechanical properties, as well as a good conductivity that was preserved also after strain cycles. Another example is represented by the electro-tendon presented in Pan et al.[35] Spider silk may also be used as a binding agent for Si-based electrodes, which seem to provide superior electrochemical performances.[36] Singh et al. produced a composite by mixing dissolved silk with Fe_3O_4, but no magnetic characterization was performed.[37] Thus, despite a certain number of hybrid spider-silk magnetic materials have been produced, there is scarce knowledge about their magnetic properties, and how these are in synergy with the mechanical ones.

In this work, we present a simple method to produce a hybrid material composed of a spider silk thread, with micrometric diameter, coated with a ferromagnetic magnetostrictive layer ($Fe_{50}Co_{50}$ alloy) (**Figure 1**a–d). The combination of these two elements results in a wire-like ferromagnetic metallic system, which retains its electrical conductivity under strain, highly flexible and extensible—so that it can be modified in shape as well as modeled to act as a component according to specific applications (Figure 1f)—and displaying good mechanical performances. Moreover, the hybrid system features magneto-mechanical coupling, i.e., its magnetic response can be varied by applying a mechanical strain, and it is able to actuate stresses that outperform many magnetic actuators. Therefore, multifunctional hybrid systems of this kind have the potential for being exploited as basic components in electronics and soft robotics applications, such as sensing or actuation.

2. Results

In this study, we used the dragline silk threads (STs) (Figure 1a) produced by *Cupiennius salei* (Keyserling 1877)[38] and composed by at least two silk fibers (Figure 1b). The STs were collected and then prepared for further characterization following the procedure reported by Blackledge et al.,[38] namely each ST was cut into pieces of the desired length and then fixed on a cardboard frame with a double-sided tape (Figure 1c). To obtain the magnetic silk threads (MSTs), the STs were covered with a 100 nm thick magnetic $Fe_{50}Co_{50}$ (FeCo) layer. The layer was deposited in Ar atmosphere (Ar pressure ≈0.1 Pa) using a high-vacuum dc magnetron sputtering apparatus (base pressure ≈10^{-5} Pa; Figure 1d,e). Due to that, as a control, vacuum silk threads (VSTs) were also prepared by exposing the STs to a high vacuum stage comparable to that used for the MSTs preparation.

2.1. Scanning Electron Microscopy

Figure 2 shows representative scanning electron microscopy (SEM) images recorded on an MST sample after performing the tensile tests, by collecting both secondary (Figure 2a,b) and backscattered (Figure 2c,d) electrons. The morphology of the MST was not significantly affected by the coating procedure, and was similar to that of ST (Figure 1b). The quality of the coating was also investigated with SEM backscattered electrons detector. In particular, the compositional contrast (Figure 2c,d) appeared uniform and the Energy dispersive X-ray spectroscopy (EDXS) analysis (Figure S1, Supporting Information) confirmed the presence of the FeCo layer. These results indicate that the FeCo coating of each of the silk fibers composing the thread was uniform.

The diameter of the threads was measured by means of optical microscopy. The average diameter value is 9 ± 5 µm for both MSTs and VSTs, while for the STs the measured value is 11 ± 5 µm. The typical size of a single silk fiber, as obtained by SEM measurements, is ≈1 µm.

2.2. Electrical Conductivity

The results of the electrical conductivity measurements are presented in **Figure 3**. Figure 3a shows a representative potential difference–current curve (i.e., ΔV versus I), measured on 5 mm long MSTs. The trend is linear, and the same is found for negative current values, which is consistent with an ohmic type conduction. The obtained electrical resistance value, i.e., the slope of the ΔV versus I curve, was $R_{MST} = 11.13 \pm 0.03$ kΩ. Figure 3b reports the ΔV versus eng. strain ε dependence for the MST sample when $I = 7$ µA. Two different regimes are observed: at first, ΔV increases linearly, tripling its value, on increasing the applied strain up to ≈0.02; at higher strain, ΔV is nearly constant and reaches a plateau value till the fracture of the magnetic layer, and thus loss of continuity, at $\varepsilon = 0.08$. In these experiments, a selected maximum strain was cyclically applied in order to verify that the conductivity did not drop to zero, i.e., the coating was not stripped (if the strain was lower than 0.08). More details on the effect of the cyclic loadings on the electrical conductivity of the MSTs are reported in Supporting Information Section S2.

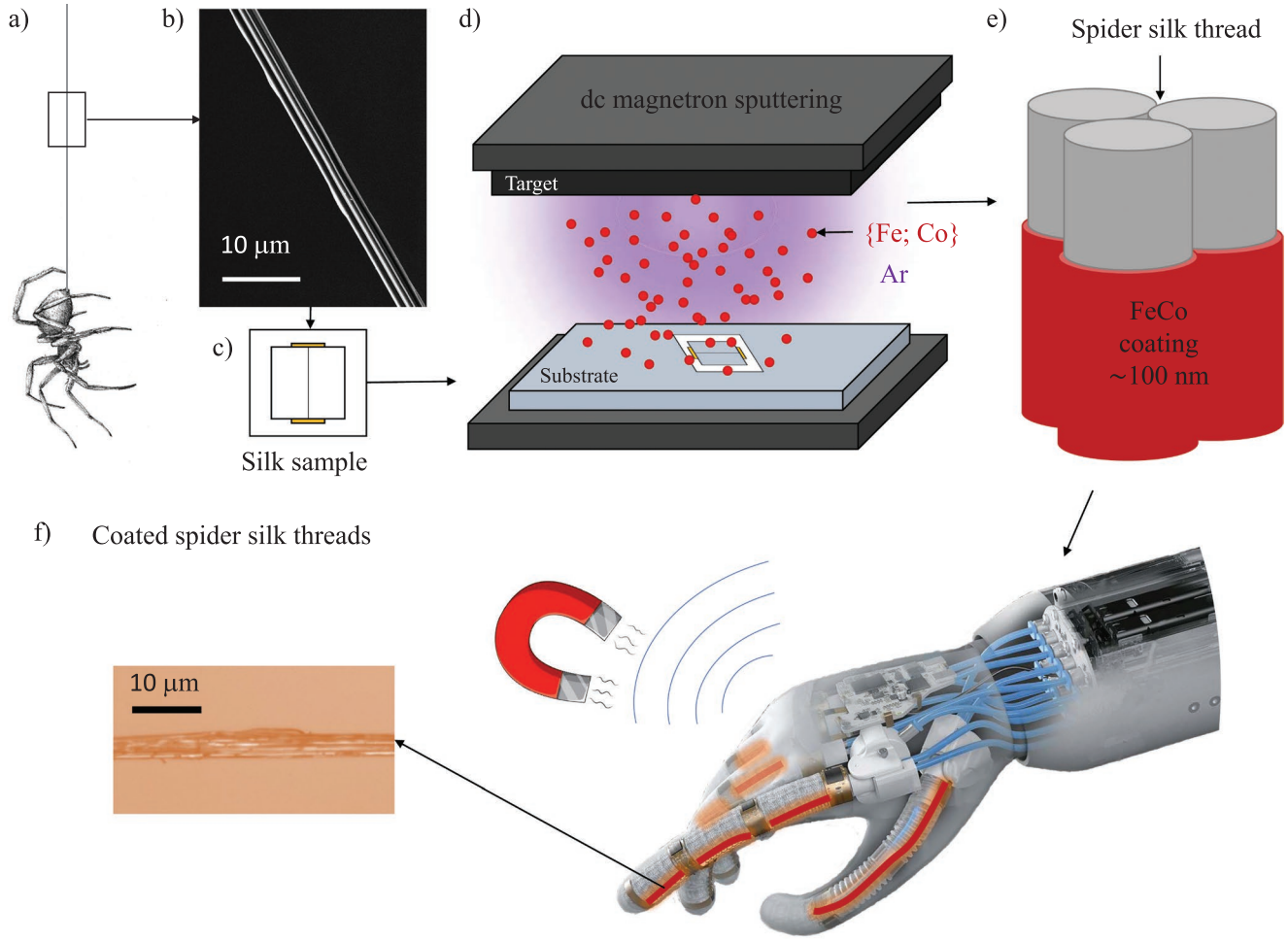

Figure 1. Schematic of the sample preparation. a) The silk samples were collected from dragline threads naturally spun by the spider. b) Scanning electron microscopy image of the native silk thread. c) The samples were mounted on a paper frame and then d) they were sputtered with magnetic coating. e) The silk threads were sputtered homogeneously with a coating of ≈100 nm in thickness. f) The hybrid materials obtained in this way are suitable for being used as micro-components in soft-stretchable electronic devices (adapted from festo.com).

2.3. Mechanical Characterization

Tensile tests were performed on both STs and MSTs. The transformation of STs in MSTs involved two steps, namely the permanence in a high vacuum chamber and the deposition of the FeCo coating (section "Spider Silk Coating"). Therefore, to disentangle the effect of the two steps on the mechanical properties and to pinpoint the contribution of the metallic layer, we also prepared an additional set of samples, VSTs. VSTs were obtained by exposing the STs to a high vacuum stage comparable to that used for the preparation of the MSTs, i.e., they were kept at 10^{-5} Pa for ≈50 min. **Table 1** and **Figure 4** display the results of the mechanical characterization (the *p*-values of the pairwise comparisons are listed in Tables S1–S4, Supporting Information). The mechanical properties and the diameters of the raw material, ST, are comparable to those reported in the literature and display the same inherent variability.[22,23,26,39–41] The permanence in high vacuum seemed to plasticize the threads by improving their deformability (the strain at break of the VSTs was significantly the highest) whereas the presence of the metallic coating seemed to slightly reduce it. Moreover, the high vacuum stage also seemed to have a marked effect on the mechanical properties of the fibers (strength, especially), as the STs presented the highest strength in comparison to the MSTs and VSTs. Nevertheless, the Young's modulus of the MSTs was the same as the native ones and only the VSTs were significantly softened. The highest toughness was the one of the STs, probably due to the strength reduction observed for both MSTs and VSTs. Lastly, we found that, for the three groups of samples, in particular the VST and the MST ones, the strength and the Young's modulus are negatively correlated with the diameter (Figure S3, Supporting Information), as is usually observed in silk fibers.[42]

The maximum likelihood method[22,43] was used to calculate Weibull parameters for the three types of tested samples (scale and shape; Table 1). The strength Weibull distributions of the samples are depicted in Figure 4f, and the narrower one belonged to the coated samples, which indicates a more homogeneous behavior in terms of fracture.[22]

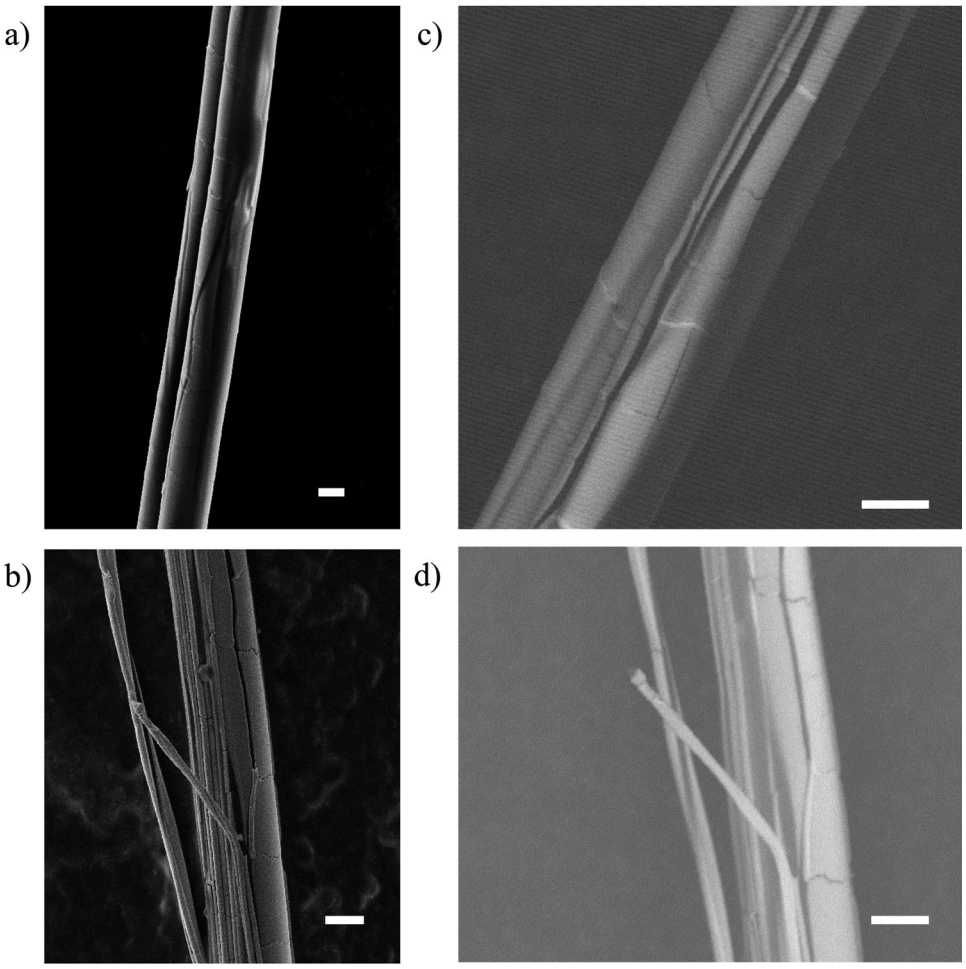

Figure 2. SEM images of a MST sample, recorded after tensile tests, and obtained collecting secondary electrons (a,b) or backscattered electrons (c,d). The scale bar corresponds to 2 µm.

2.4. Magnetic Properties

In addition to the MSTs, we also prepared a reference magnetic sample by sputtering a 100 nm thick FeCo film on a planar naturally oxidized silicon substrate, under the same experimental conditions adopted for coating the STs. This reference film was labeled as $FeCo_{ref}$.

Figure 5a shows the magnetic hysteresis loops measured by superconducting quantum interference device (SQUID) magnetometry on $FeCo_{ref}$, at room temperature, by applying the

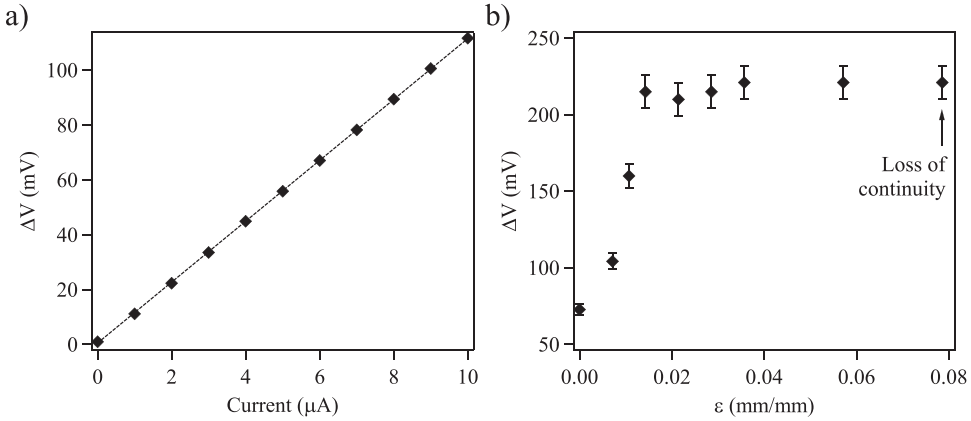

Figure 3. a) ΔV–I curve of the MST measured in the lab; the electrical resistance value obtained from the slope of the linear dependence is $R_{MST} \approx 11$ kΩ. b) Graph of the potential difference measured on the MST versus the eng. strain ε applied to it.

Table 1. Mechanical properties and Weibull parameters of the tested samples.

Type of silk	Diameter [μm]	Strain at break [mm mm^{-1}]	Strength [MPa]	Young's modulus [GPa]	Toughness modulus [MJ m^{-3}]	Scale Parameter [MPa]	Shape Parameter
ST	11 ± 5	0.28 ± 0.10	365 ± 290	5.2 ± 4.8	61 ± 46	382	1.41
MST	9 ± 5	0.23 ± 0.18	102 ± 85	4.9 ± 3.7	22 ± 24	111	1.33
VST	9 ± 5	0.63 ± 0.22	93 ± 88	2.0 ± 1.9	29 ± 19	85	1.03

magnetic field H along two arbitrary orthogonal directions in the plane of the film, labeled as $\theta = 0°$ and $\theta = 90°$. The obtained loops are squared, which indicates that the magnetization lies in the plane of the film under the prevailing action of the shape anisotropy. However, the shape of the loops does not depend on the applied field orientation, i.e., the sample is magnetically isotropic in the plane. The saturation magnetization of the film is $M_S = 1.75 \times 10^6$ A m^{-1}, the coercivity H_C is ≈11.5 kA m^{-1} and the irreversibility field H_{IRR}, i.e., the field value at which the two branches of the loop join, is ≈12.7 kA m^{-1} (**Table 2**). The M_S value is slightly smaller than that of bulk FeCo (i.e., 1.91×10^6 A m^{-1}),[44] which can be due to a partial oxidation of the FeCo layer and/or to a mass density reduction often observed in sputtered thin films.[45] Differently, both H_C and H_{IRR} are very high with respect to the bulk ones that, for the ordered alloy, are of the order of 1 Oe.[44] The analysis performed by magneto-optic Kerr effect (MOKE) magnetometry on $FeCo_{ref}$ confirms the H_C and H_{IRR} values obtained by SQUID.

Figure 5b shows the hysteresis loop measured by SQUID on the MSTs with H applied parallel to their long axis. To increase the intensity of the magnetic signal, three 5 mm long MSTs were measured at the same time. The measured magnetic moment at saturation is $\mu_{sat} = 7.74 \times 10^{-8}$ A m^2; H_C is ≈23.9 kA m^{-1} and H_{IRR} ≈43.8 kA m^{-1}, higher than those measured on $FeCo_{ref}$. If we approximate each MST by a ferromagnetic microtube with length of 5 mm, diameter of 9 μm (Section 2.1), thickness of 100 nm, with a M_S equal to the $FeCo_{ref}$ one, the expected magnetic moment for three MSTs is 7.5×10^{-8} A m^2. This result

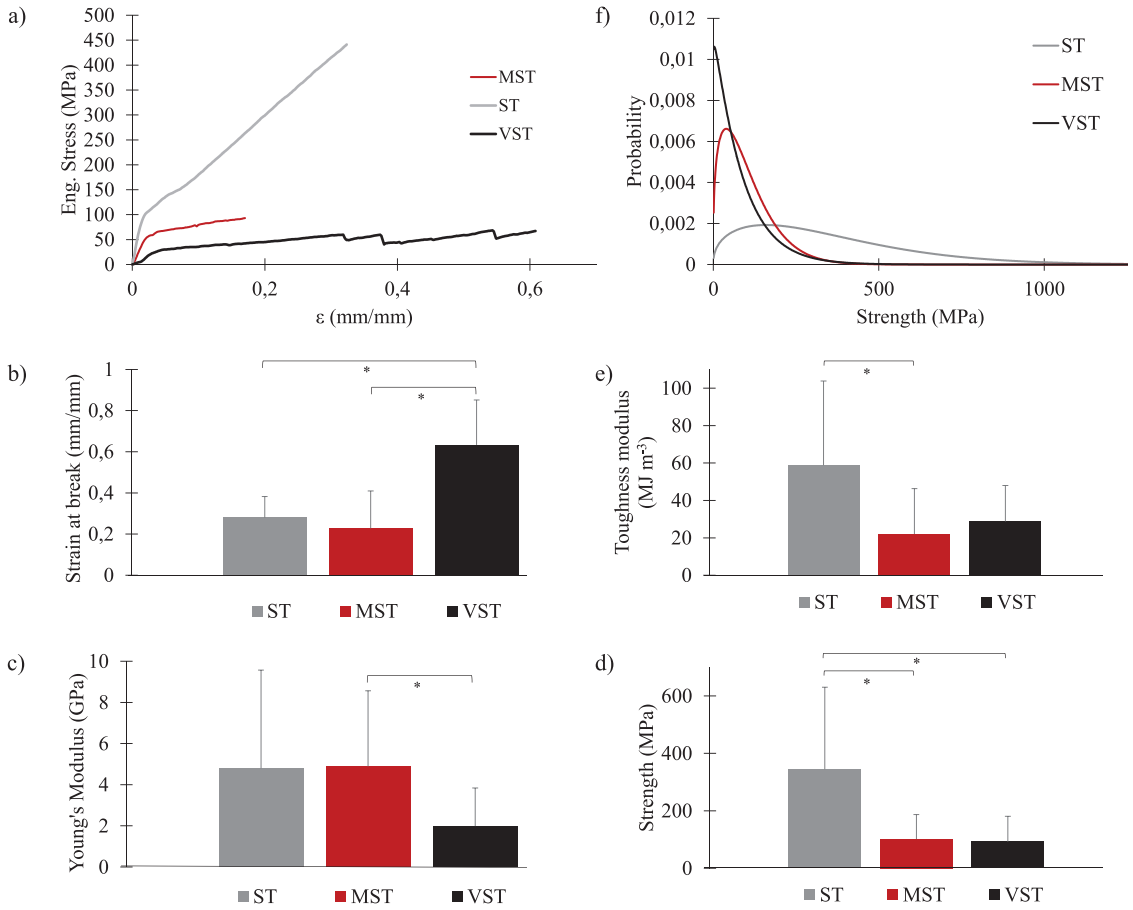

Figure 4. a) Representative engineering stress–engineering strain curves of the tested samples. b) Strain at break, c) Young's modulus, d) strength, and e) toughness modulus of the tested samples. f) Weibull distribution of strength of the analyzed samples. Stars indicate that the difference is significant (p-value < 0.05).

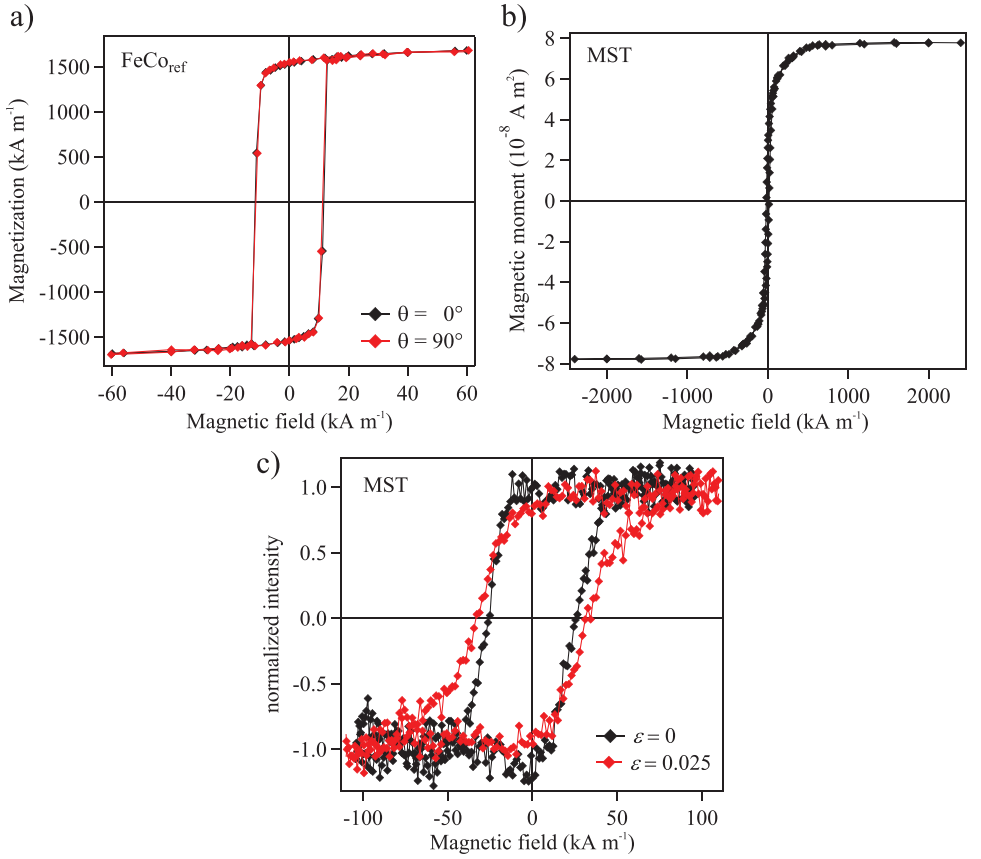

Figure 5. a) SQUID magnetic hysteresis loops measured at room temperature on the reference 100 nm thick FeCo film (FeCo$_{ref}$) with the external field applied parallel to the plane of the film, along two arbitrary orthogonal directions, labeled as $\theta = 0°$ and $\theta = 90°$. b) SQUID magnetic hysteresis loop measured at room temperature on three MSTs with the applied field parallel to the MSTs direction. c) Comparison between the MOKE signal recorded on an unstrained MST (full black symbols) and the MOKE signal collected on an MST subjected to an engineering strain $\varepsilon = 0.025$ (full red symbols). In both cases, the direction of the applied magnetic field is parallel to the MST and the measurements were performed at room temperature.

is close to the measured one, thus supporting the fact that the MSTs display a bundle structure and suggesting that the FeCo coating maintains its M_S value.

We also performed a magnetic characterization using MOKE magnetometry. The loops measured on a single MST (with H parallel to its long axis) with no strain (i.e., $\varepsilon = 0$) and under a tensile strain $\varepsilon = 0.025$ are shown in Figure 5c. We used a small strain value in order to reduce cracks formation.[46–48] In the unstrained condition, the magnetization reversal process is less sharp than that observed in FeCo$_{ref}$ (Figure 5a) and even less in the strained state. The values of H_C and H_{IRR} increase considerably when passing from the unstrained to the strained state. MOKE measurements were also performed after subjecting MSTs to cyclic tensile loadings, to check if this procedure affected the magnetic properties. More details about this point are reported in Supporting Information Section S2.

2.5. AFM and MFM Analysis

A combined atomic force (AFM) and magnetic force (MFM) microscopy analysis of the MSTs was performed in order to access both their morphology and their magnetic configuration. **Figure 6**a confirms the bundle structure of the MST.

Table 2. Coercivity H_C and irreversibility field H_{IRR} values for the different samples. H_C and H_{IRR} for the bulk case were obtained from Ref. [44].

Samples	Method	H_C [kA m^{-1}] ± 2%	H_{IRR} [kA m^{-1}] ± 2%
FeCo bulk	Ref. [44]	≈0.1	≈0.1
FeCo$_{ref}$	SQUID/MOKE	11.5	12.7
MST	SQUID	23.9	43.8
	MOKE	25.5	46.2
MST, $\varepsilon = 0.025$	MOKE	32.6	75.6

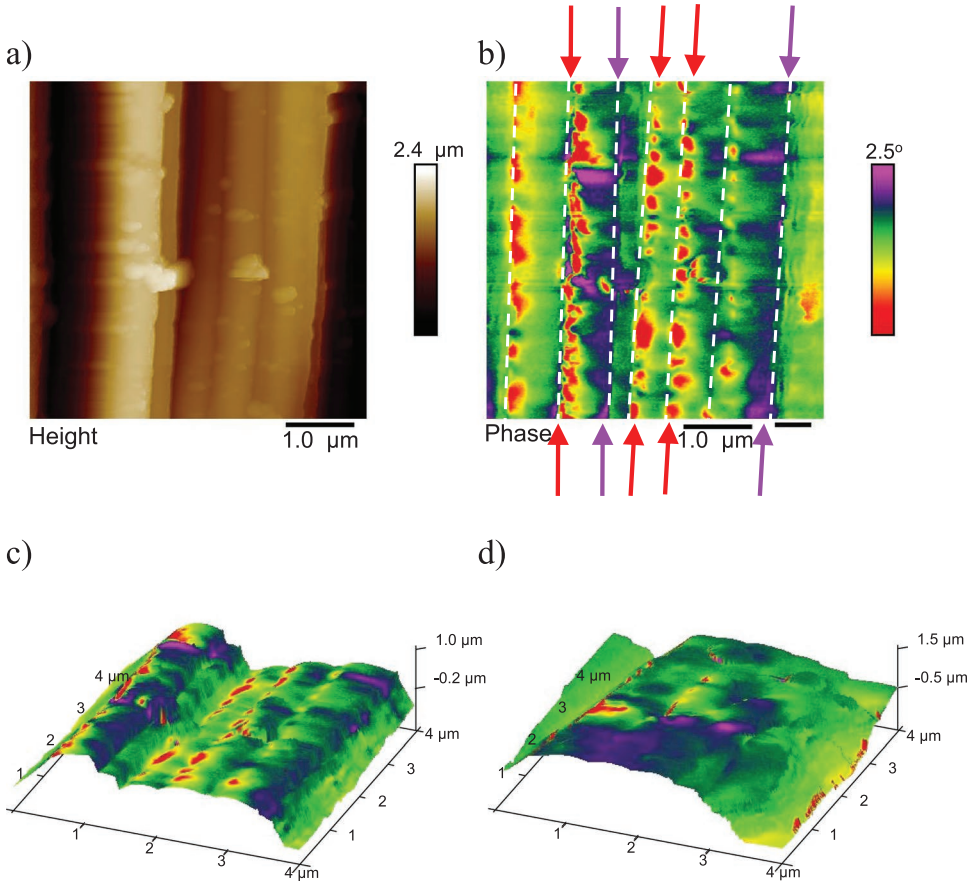

Figure 6. a) AFM and b) MFM maps recorded on a region of a MST where the presence of the bundle structure can be clearly observed. In (a), some sub-micrometric particles, probably dust, can be observed. In (b), the white dashed lines represent the lateral sides of the fibers; each red (violet) arrow points to the side close to which the regions characterized by a red (violet) MFM contrast are located. Comparison between the 3D magnetic reconstructions, resulting from the combination of the 3D morphology, as obtained from AFM profiles, and of the magnetic contrast, as obtained from MFM profiles, of the unstrained MST (c), and of the same MST whilst that is strained ($\varepsilon = 0.025$) (d). Regarding the magnetic phase contrast, panels (c) and (d) share the color scale reported in panel (b).

The FeCo layer, which seems to cover the fibers in a rather uniform fashion, presents a smooth surface, with a mean roughness of ≈3 nm (see also Figure S4, Supporting Information). In Figure 6b, the MFM profile of the same sample region is displayed. Areas showing a pronounced magnetic contrast are aligned near the grooves between adjacent fibers. In more detail, areas displaying a negative (red) contrast are found on one side of the fibers and those showing a positive (violet) contrast are located on the opposite side. Differently, in the other portions of the fibers (i.e., making reference to the height scale, at the top of each fiber) the contrast appears to be smoother.

We also performed the AFM-MFM analysis in a strained condition equal to that used for MOKE measurements (i.e., $\varepsilon = 0.025$). The effect of the strain can be well appreciated by comparing the 3D maps displayed in Figure 6c,d. In these maps the MFM signal has been superimposed to the morphology of the MST, reconstructed using the AFM map, in order to better highlight the position where a specific MFM signal is detected. Figure 6c refers to the $\varepsilon = 0$ case, while Figure 6d to the $\varepsilon = 0.025$ one. Overall, in Figure 6d, there is a strong reduction of the magnetic contrast at the sides of the fibers with respect to Figure 6c.

2.6. Magnetic Actuation

The magnetic actuation was evaluated by clamping the MST in the nanotensile machine at fixed distance (the MST were in tension at 0.5%) and by measuring the load while the commercial magnets were approached to the sample (**Figure 7**a). The magnetic configuration of the commercial magnets is presented in Figure 7b, while the dependence of the intensity of the magnetic induction B as a function of the distance from the magnets, measured along the magnets to MST direction (represented by the green arrow in Figure 7b), is displayed in Figure 7c (Video S1, Supporting Information). The B intensity changes rapidly as the distance is varied, thus revealing the non-uniformity of the B configuration. This conclusion is also supported by the B intensity map displayed in Figure S5b (Supporting Information). The load increases with the approaching of the magnets (Figure 7b) up to a value of 0.12 mN that, considering that the diameter of the used thread was ≈5 µm, corresponds to a maximal stress of ≈10 MPa. That value was measured when the magnet was almost in contact with the MST (distance ≈0 cm), and it was cyclically consistent upon different approaches (Figure S6, Supporting Information).

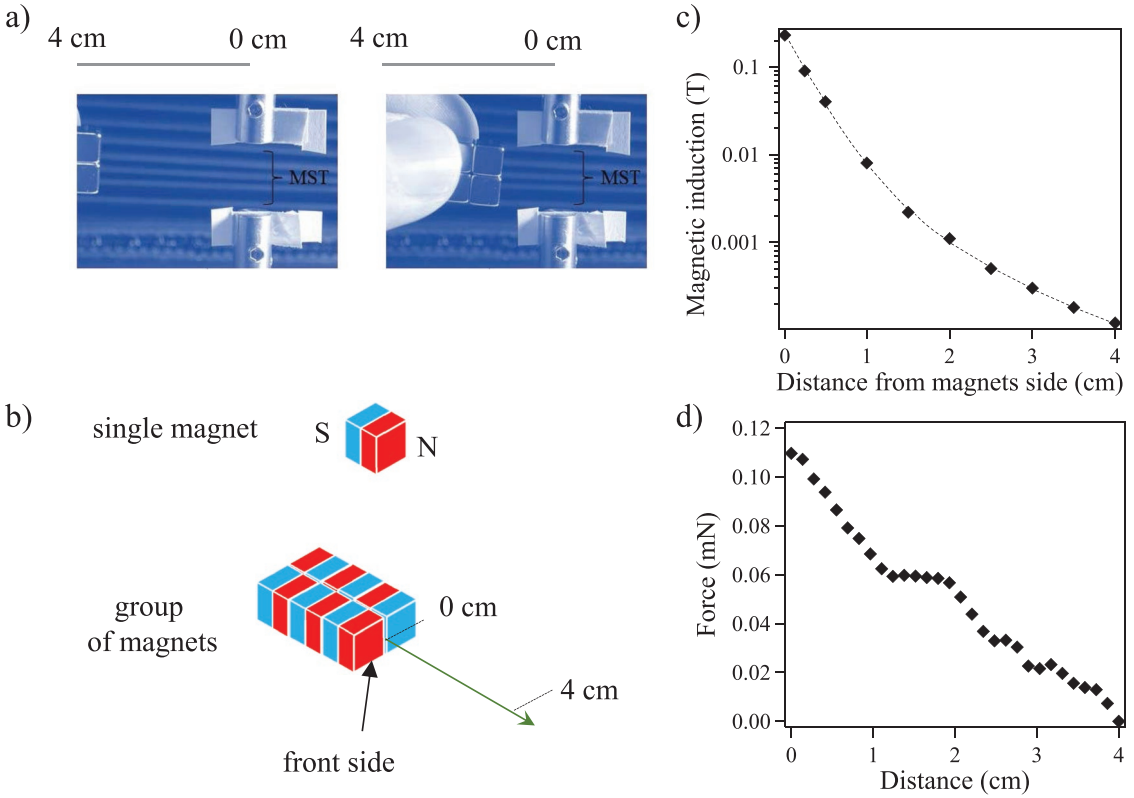

Figure 7. a) Scheme of the experimental setup used to access the effect of the actuation induced by the magnets on MSTs. Starting from a distance of ≈4 cm, the commercial magnets were approached till almost the contact with MST. b) Representation of the north (N/red) and south (S/blue) poles configuration of a single commercial magnet (upper part), and of the group of magnets used for the experiment (lower part). c) Dependence of the magnetic induction intensity, measured along the path represented by the green arrow in panel (b), as a function of the distance from the front side of the group of magnets. The dotted line is a guide to the eye. d) Nanotensile machine load on the MST as a function of the distance of the commercial magnets from the MST.

3. Discussion

In this work, spider silk threads have been collected and used as a basic material in view of the production of micromagnetic multifunctional devices. This has been done by coating the samples with a 100 nm thick magnetostrictive FeCo layer.

The FeCo coated threads retained their original shape, which is essentially cylindrical, albeit with a bundle morphology (Figure 2). Only a small reduction in diameter was observed, in agreement with literature's results (decrease of ≈10%) and due to the dehydration of the sample during vacuum exposure.[49,50] The stability over time and uniformity of the FeCo coating were assessed by EDXS and SEM analyses. The coating was seen to cover the fibers also after the mechanical tests, i.e., after breaking the MSTs. These results support the good silk-FeCo coating adhesion.

Electrical resistivity values, measured both on strained and unstrained MSTs, are of the order of 10^4 Ω, suitable for many electronics applications.[9] For comparison, we estimated the resistance, R_{th}, of a MST modelled as a cylinder with length 5 mm, diameter 9 µm (see Section 2.1), and uniformly covered with a 100 nm thick FeCo layer. Since the resistivity measured on the $FeCo_{ref}$ film was 30×10^{-8} Ω m, from the second Ohm's law we obtained R_{th} = 0.5 kΩ, which is lower than R_{MST}. Due to shadowing effects related to the sputtering deposition method,[51] the thickness of the FeCo layer in the interstices between adjacent fibers may be lower than the nominal value. As a consequence, the value of R_{th} could be underestimated. Moreover, the high R_{MST} value suggests that the FeCo coating, grown on a flexible substrate, most likely has a higher defect density and therefore a higher resistivity compared to the $FeCo_{ref}$ film, which was deposited on a rigid planar substrate.[52] On the other hand, the presence of defects does not imply the existence of a significant number of discontinuities in the FeCo coating. In fact, in that case, both a much higher resistance value and a non-linear ΔV versus I curve would be measured.[53,54] Hence, the R_{MST} value is in favor of a metallic covering providing a good degree of electrical continuity.

For comparison, a resistance as high as $\approx 10^5$ Ω was measured on ≈20 mm long spider silk threads coated with a 100 nm thick gold layer.[32] Electronic devices based on spider silk were also designed by hybridizing it with graphene (with a resistivity circa ten times higher than that of MST[33]) and carbon nanotubes.[34,35] In these systems, resistance values similar to those measured in our MSTs were obtained when the temperature was several degrees below 0 °C. Moreover, the resistance of carbon nanotubes-based devices was seen to increase tremendously with the strain. In particular, at 10% of strain the resistance was over 1 MΩ, which is almost 90 times the value

found for the MSTs at a similar level of strain (≈33 kΩ at 8% of strain, Figure 3). The initial increase in resistivity that was here observed is in agreement with other authors when applying a tensile strain to samples produced by growing a metallic film on a planar elastic substrate. This effect was ascribed to the formation of cracks in the metallic layer,[47,55] and the relative variation of resistance was of some orders of magnitude.[47] In our case, cracks may develop starting from the interstitial regions between adjacent fibers, where the thickness of the FeCo film is smaller, with respect to the other parts of the thread, and so the stress on it is higher.[56] In this way, resistance increases but electrical continuity is preserved. It is expected that, as the strain increases, the cracks density reaches a constant value,[47,48,57] and therefore the resistance does not change further, as indeed observed in our case. Eventually, when the strain is ≈0.08, cracks may appear orthogonally to the fibers,[47,57,58] and/or the thread may fray, so the electrical continuity is lost. This value of the upper strain limit for electrical conduction is higher with respect to those reported in literature related to similar systems.[32,33] In summary, these data highlight the potential of the MSTs, as useful resistance values are obtained at room temperature and no variation of the order of magnitude is produced under strained conditions.

As for the mechanical performance, with respect to the STs, the MSTs exhibited comparable values of strain at break and Young's modulus, and smaller values of toughness modulus and strength (Figure 4). The same Young's modulus values could be explained by the presence of the stiff magnetic coating, which could have compensated the plasticization induced by the vacuum. The observed modifications may be ascribed to different factors: the presence of the metallic coating, the exposition of the silk fibers to a high vacuum environment, the energy released by the impinging atoms during the sputtering process. The contribution of this last mechanism was considered negligible, since the atoms sputtered from the FeCo target have an average energy of ≈1 eV.[59,60] They nearly have the same energy when impinging on the silk fibers as, due to the low Ar pressure (≈0.1 Pa), the energy reduction due to the thermalization with Ar atoms is negligible.[60] For confirmation, we radiated the fibers with the electron beam of the SEM apparatus using different values of the accelerating voltage. As shown in Figure S7 (Supporting Information), the beam starts to damage the fibers when its energy is ≈3.4 keV, much larger than the energy of the impinging atoms.

Regarding the influence of low pressure on mechanical properties of spider silk, Ene et al.[61] noticed that in the silk of *Trichonephila* sp. (former *Nephila* sp.), an increase in pressure led to a more organized level in the amorphous phase of the protein (which is likely to be related to an increase in strength[42,62,63]). Thus, it is likely that the permanence in a high vacuum environment was the main cause of the experienced decrease in silk's strength. On the other hand, the metallic coating could bring about the decrease in extensibility (since its fragile nature). Overall, despite the mechanical performances of MSTs have not improved, with respect to STs ones, they are still acceptable for common applications,[9,10,12] and also for most soft electronics components and better than common hybrid composites obtained with silkworm silk.[19]

The study of the magnetic properties of the MSTs disclosed the magneto-mechanical effects deriving from of the interplay between the silk and the magnetostrictive FeCo layer.

The large H_C and H_{IRR} values of the $FeCo_{ref}$ sample are an indication of the presence of internal residual stresses, induced by the growth process.[64,65] Since FeCo is a magnetostrictive alloy, these stresses induce the appearance of a net magnetoelastic anisotropy contribution, K_E, to the total magnetic anisotropy of the film. From the analysis of the magnetic hysteresis loops measured on $FeCo_{ref}$ with the field applied both in-plane (Figure 5a) and out-of-plane (Figure S8, Supporting Information), we estimate that $K_E \approx 8 \times 10^4$ J m^{-3}, corresponding to a stress magnitude of ≈900 MPa (see Supporting Information Section S4 for more details). Regarding the MSTs, both SQUID and MOKE analyses showed that there is a further increase in H_C and H_{IRR} with respect to those of the reference sample $FeCo_{ref}$. This is consistent with an enhanced magnetic anisotropy of the MSTs.

The anisotropy increase may be determined by the existence of two possible contributions: i) a shape anisotropy term, which may originate from the particular morphology of the MSTs, i.e., an elongated structure with a curved profile[66–68] in the form of a bundle; ii) an increase in the strength of the internal stresses, and therefore of the magnetoelastic anisotropy term, which may arise from the mechanical coupling with the silk thread. Certainly, the latter is a much more irregular structure compared to the flat Si substrate on which the $FeCo_{ref}$ film is grown. Moreover, after the coating is deposited, the silk fibers exit the vacuum chamber and are subjected to a huge change in relative humidity, which modifies both their mechanical properties and tensional state.[29,69]

To assess the impact of these different anisotropy contributions on the hysteretic behavior and magnetic configuration of the MSTs, micromagnetic simulations were carried out using MuMax^3, a GPU-accelerated micromagnetic simulation program developed at Ghent University and exploiting the finite difference method.[70–72]

The MST was modeled as depicted in **Figure 8**a: it is a bundle of three cylinders, each with an internal radius R_I of 500 nm, a length L of 400 nm, and a thickness of 100 nm. To take into account the contribution of shadowing effects related to sputtering deposition,[51] the thickness of the magnetic layer in the grooves between adjacent fibers was reduced (Figure 8b). The saturation magnetization M_S value measured on $FeCo_{ref}$ was used as reference. More details on the simulation methods are given in Supporting Information (Section S5).

As a first step, the micromagnetic calculation was carried out taking into account only the shape anisotropy contribution. The hysteresis loop was calculated considering that the magnetic field H was applied parallel to the z axis. The result is shown in Figure 8c. The values of H_C and H_{IRR} are 9.15 and 9.55 kA m^{-1}, respectively, less than 50% of the measured values (Table 2). This indicates that the shape term is not sufficient to account for the observed magnetic hardening of MST with respect to $FeCo_{ref}$.

Then, the case in which a magnetoelastic anisotropy contribution was also present was simulated. Since the exact configuration of the internal stresses in the FeCo coating was obviously unknown, we assumed that the local orientation of the

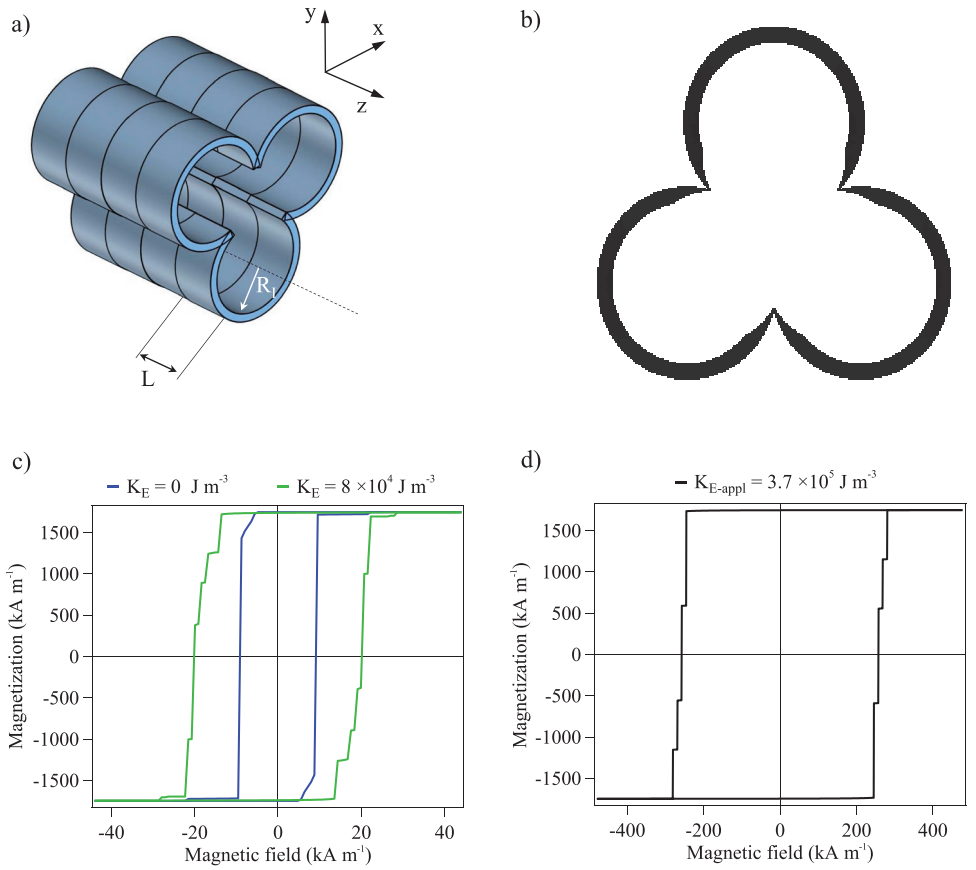

Figure 8. a) Representation of the bundle of three cylinders, in contact with each other, with an internal radius R_I of 500 nm, a length L of 400 nm, and a thickness of 100 nm. For better viewing, four replicas of the bundle are displayed. b) Actual cross section of the bundle represented in panel (a), highlighting the reduction of the thickness of the FeCo layer in the interstices between adjacent fibers. c) Hysteretic behavior of the bundle when considering only the contribution of the shape anisotropy (straight blue curve) or when also the contribution of the magnetoelastic term, having a local orientation that changes and $K_E = 8 \times 10^4$ J m^{-3}, is included (green straight curve). d) Hysteretic behavior when the magnetoelastic term has an orientation parallel to the z axis and $K_{E\text{-appl}} = 3.7 \times 10^5$ J m^{-3}.

magnetoelastic anisotropy axis changed while the value of K_E was the same everywhere. Assuming $K_E = 8 \times 10^4$ J m^{-3}, i.e., that estimated for the $FeCo_{ref}$ film (corresponding to a stress magnitude of 900 MPa), with respect to the previous case increased H_C and H_{IRR} (19.9 and 28.6 kA m^{-1}, respectively) are obtained (Figure 8c). Nevertheless, they are still smaller than the measured ones, which supports that the coupling of the FeCo layer with the silk leads to a value of K_E larger than that of the $FeCo_{ref}$ film.

The micromagnetic simulations allow to calculate also magnetic configurational maps, from which maps displaying the corresponding MFM contrast can be calculated. As for the hysteresis loops, two cases were considered, i.e., without and with magnetoelastic anisotropy, namely without and with internal stresses (more details in the Supporting Information Section S6). The results (Figure S10a,b, Supporting Information) reveal that in the first case the magnetic configuration is uniform and no MFM contrast is visible, while a magnetic contrast of variable sign appears at the sides of the fibers when the magnetoelastic anisotropy is included in the calculation. This last finding is in line with the experimental results of Figure 6b and therefore confirms the presence of a non-uniform local stress pattern in the FeCo coating.

When the MSTs are subjected to a tensile strain ($\varepsilon = 0.025$), differences in the hysteresis loop shape (Figure 5c) and in the MFM map (Figure 6d) are clearly observed with respect to the unstrained case, indicating the existence of a drivable magneto-mechanical coupling between the silk core of the thread and the magnetostrictive FeCo coating. To simulate the influence of the strain on the magnetic properties of the MST, we needed to estimate K_E. However, the evaluation of the magnitude of the actual applied stress, which produces the strain $\varepsilon = 0.025$, is not straightforward. In fact, when a strain is applied to a flexible substrate covered by a metallic layer, the strain may not be uniform along the thickness.[56,73] The applied stress can be roughly estimated as $\sigma_{appl} = E_{FeCo} \times \varepsilon$, where E_{FeCo} is the Young modulus of FeCo. Assuming E_{FeCo} = 165 GPa, i.e., the value expected for thin FeCo layers,[74,75] we obtain σ_{appl} = 4.1 GPa. This value is ≈4.5 times larger than that of the internal stresses (i.e., 900 MPa) used in the previous simulations of the unstrained MST. Therefore, the micromagnetic calculations were carried out assuming that the magnetoelastic anisotropy term associated to σ_{appl}, i.e., $K_{E\text{-}appl} = 3.7 \times 10^5$ J m^{-3}, is the leading one and the contribution related to the internal stresses can be disregarded.

The obtained hysteresis loop is reported in Figure 8d, H_C and H_{IRR} are 255 kA m^{-1} and 279 kA m^{-1}, respectively. Hence the two parameters increase with increasing ε, an effect confirmed by the experiments, although the measured values of H_C and H_{IRR} are definitely lower (Table 2) probably because σ_{appl} is overestimated.

The calculated MFM map, displayed in Figure S10c (Supporting Information), shows just a feeble magnetic contrast. Therefore, the application of a tensile stress to MST results in an overall more uniform magnetic configuration, as experimentally observed (Figure 6d).

Finally, the magnetic actuation of MST was investigated by measuring the tensile force generated on the thread when a group of magnets was approached. The generated load, and also the corresponding stress, were larger than those produced by typical biomedical magnetic actuators.[76,77] Moreover, MST was repeatedly bent under actuation with a degree desirable in magnetic actuators for soft robotics applications (Video S2, Supporting Information).[78] For example, in Gao et al.,[79] flexible magnetic microelectrodes generated a stress of about a few MPa when exposed to a variable magnetic field, comparable to what was here achieved with only one thread, thus the MSTs display properties that are suitable for such applications.[80] These results highlight the potentiality of using hybrid systems of this kind as basic components for magnetic actuators.

4. Conclusions

Soft robotics and electronics are fast-moving fields, in which every day new materials emerge, as well as new needs. Among these, the necessity of having flexible electrical fabrics that retain the mechanical efficiency and the electrical properties is commonly highlighted. The magnetic properties are an added value that can be used to generate actuation, improve the interface with the device, perform sensing, and store information. To achieve such needs, new types of highly performant composite fibers are to be designed.

In this work, we present a new spider-silk based material with a strong multifunctional nature. Despite the treatment, the spider silk fibers nearly preserved their natural mechanical properties, but also gained additional functionalities, namely stress-sensing magnetic properties, thanks to a magneto-mechanical coupling between the silk core of the thread and the magnetostrictive FeCo coating, and a strain-dependent electrical conductivity. This hybrid system has been here characterized from mechanical, magnetic, and electrical point of views, providing a solid proof of concept of this functional engineered spider silk. This fiber could be used as a component in soft electronics/robotics and sensing composites nearly as it is, or used as a proof for further investigations with other type of fibers including the relevant example of artificial spider silk, which can be now produced at large scale.[81]

5. Experimental Section

Silk Collection: The spider silk studied in this work was produced by *Cupiennius salei* (Keyserling 1877).[41] The spiders were kept in different glass or plastic terrariums and fed with a weekly diet of insects (*Blaptica dubia* or *Acheta domestica*). All the terrariums were set in a room with controlled environmental parameters. Each terrarium was provided with a small refuge by considering the needs of the animal, according to the Italian regulation on animal protection and EU Directive 2010/63/EU for animal experiments. The spider, during its walking inside the terrarium, continuously produced dragline silk threads (Figure 1a), which were composed by at least two silk fibers (Figure 1b). These threads, whose length was of approximately 20 cm, were collected and consequently cut into smaller pieces and then prepared for further characterization.

Spider Silk Coating: The samples were prepared by following the procedure reported by Blackledge et al.[38] Briefly, each ST was cut into pieces of the desired length using scissors, and each specimen was then placed on a cardboard frame provided with a window of 0.75 cm × 0.75 cm and fixed with a double-sided tape (Figure 1c). To obtain the MSTs, the STs fixed in the cardboard frame were coated with a 100 nm thick magnetic layer made of a FeCo alloy (Figure 1d,e). The magnetic layer was deposited with a custom-made high-vacuum dc magnetron sputtering apparatus[82] in Ar atmosphere (Ar pressure ≈0.1 Pa, base pressure ≈10^{-5} Pa) using a high purity FeCo sputtering target. The nominal value of the thickness of the films was measured with a quartz microbalance system based on 6 MHz gold plated crystal, a Vaqtec Oscillator Kit, and an MS-9150 Metex Universal System. During the deposition process, which involved an overall permanence in high vacuum conditions of ≈50 minutes, the cardboard frame was placed on a rotating sample holder so to improve the layer homogeneity. As a reference magnetic sample, a 100 nm thick FeCo film was also deposited on a planar naturally oxidized silicon substrate, under the same experimental conditions adopted for coating the STs. This reference film was labeled as $FeCo_{ref}$. The transformation of STs in MSTs involved two steps, namely the permanence in a high vacuum chamber and the deposition of the FeCo coating. Therefore, as a control, an additional set of samples, VSTs, was also prepared. VSTs were obtained by exposing the STs to a high vacuum stage comparable to that used for the preparation of the MSTs, i.e., they were kept at 10^{-5} Pa for ≈50 min.

Scanning Electron Microscopy: For the SEM morphology characterization, an FE-SEM Zeiss – 40 Supra was used. Regarding the STs, before the observation they were coated with a Pt/Pd (80:20) layer (Quorum technology, Q150T) having a thickness of ≈5 nm. All the SEM observations were performed after the tensile tests by collecting both secondary and backscattered electrons.[83,84] EDXS analysis was performed on MSTs using an EM-30 COXEM. The spectra were obtained at 20 kV, at a magnification of 10^4. The measurements were performed 2 months after the coating of the threads, so to test the durability of the coating.

Electrical Conductivity: The electrical conductivity measurements were performed on MSTs with the four-point collinear probe method, by fixing the intensity of the current flowing in the sample and measuring the potential drop. The current generator was a Keithley 2450 Sourcemeter and an Agilent 34401A Digital multimeter was used as voltage probe. Electrical contacts between the instruments wires and the MST were made possible using silver-loaded paint. For these measurements, the MSTs were detached from the cardboard frame and fixed on a sample holder that, thanks to an endless screw, allowed to extend the length of the samples. In this way, the measurements could be performed both in zero strain and in strained conditions.

Mechanical Properties: Tensile tests were carried out using a nanotensile machine (Agilent® technologies T150 UTM) with a cell load of 500 mN, nominal declared sensitivity of 10 nN for the load, and 1 Å for the displacement in the dynamic configuration. The strain rate was 1% s^{-1} (gauge length of 7.5 mm) with a frequency load of 20 Hz. Before mounting the sample, the number of fibers per thread and the diameter of each fiber were measured with an optical microscope (Zeiss Axiotech and Axiovert) and ImageJ software analysis.[85] For each group of STs, at least ten samples were tested, and the mean values ± standard deviation of strength (MPa), strain at break (mm mm^{-1}), toughness modulus (MJ m^{-3}), and Young's modulus (GPa) were

calculated from the engineering stress–engineering strain curves.[22] Briefly, for each sample the engineering stress was obtained by dividing the value of the applied force by the initial cross section of the thread. This was calculated as the sum of the cylindrical cross sections of each fiber that composes the thread, whose diameter was measured by means of light microscopy.[50] The engineering strain was obtained by dividing the displacement by the initial gauge length. Making reference to the engineering stress–engineering strain curve, the Young's modulus was evaluated as the slope of the initial (steepest) part of that curve whilst the toughness modulus as the area below the entire curve. The tensile tests were performed 2 weeks after the samples preparation.

Statistical Analysis: The values of the ultimate strength were analyzed through the support of the software Mathematica so to obtain the Weibull parameters through the maximum likelihood method.[22,43] One-way analysis of variance (pairwise comparison) was performed to compare the mechanical properties, with a significance level of 5%. The two-tailed *p*-value were computed with the support of Matlab as previously described.[22]

Magnetic Characterization: The magnetic properties of the samples were investigated by a SQUID Quantum Design MPMS-XL magnetometer operating in the 5–300 K temperature range (maximum applied field 4 MA m^{-1}, sensitivity 10^{-10} A m^2).[86]

The magnetic behavior of the MSTs was also studied with a MOKE magnetometer, using the transverse configuration setup and the intensity modulation technique.[86,87] In this case, the maximum applied field was 160 kA m^{-1}. In more detail, the direction of the MST was kept parallel to that of the magnetic field and both of them were orthogonal to the scattering plane. In this configuration, *p* polarized light produced by a He-Ne laser (wavelength $\lambda = 632.8$ nm) was focused onto the MST and the light diffused by the sample was collimated on a Thorlabs PDA55 amplified silicon detector. For the MOKE measurements, the samples were installed using the same sample holder adopted for conductivity measurements.

Atomic Force and Magnetic Force Microscopy: AFM and MFM characterizations were performed with a Bruker Multimode V Nanoscope 8 microscope, equipped with CoCr coated MESP-HR tips. Images were taken in air with the samples at their magnetic remanence, with the tip magnetized along its axis (vertical direction). During each image acquisition, the height channel was acquired in pass 1 in intermittent contact mode, and the magnetic channel was acquired in pass 2 at a constant lift scan height of 35 nm (≈1 Hz acquisition, 384 lines). For these measurements, the samples were installed using the same sample holder adopted for MOKE measurements.

Magnetic Actuation: The mechanical response of the MSTs was evaluated through a custom-made setup. A nanotensile machine (Agilent technologies T150 UTM) was used to measure the load response of the samples and a commercial set of cubic (lateral side of 5 mm) Nickel plated N42 NdFeB magnets (by Webcraft GmbH) was used to expose the MST to a non-uniform *B* field, so as to apply a drag force to the sample.[88] The *B* intensity was measured using a FW-Bell 9500 Gaussmeter using a 1-axis Hall probe.

Each MST was set on a 0.5% level of strain and held for 120 s. After the relaxation, a static configuration was kept (the grips held the sample by measuring its mechanical response) and the MST was gradually exposed to the magnetic field by slowly approaching the cubic magnets to the MST. Their relative distance was measured by means of a Sony Camera HD. This procedure was repeated several times for each MST sample and for STs, as well, that were used to have a reference background signal, which was then subtracted from MST data.

Supporting Information

Supporting Information is available from the Wiley Online Library or from the author.

Acknowledgements

The authors would like to thank Lorenzo Moschini, Prof. Antonella Motta and Prof. Claudio Migliaresi (Biotech – Mattarello, University of Trento) for their support with SEM images and Mirco D'Incau for the support with EDXS analysis. N.M.P. was supported by the Italian Ministry of Education, University and Research (MIUR) under the PRIN-20177TTP3S grant. G.G. was supported by Caritro Foundation (prot. U1277.2020/SG.1130). F.S. was supported by the University of Ferrara under project "Fondo per l'Incentivazione alla Ricerca" (FIR) – 2021.

Open access funding provided by Universita degli Studi di Ferrara within the CRUI-CARE Agreement.

Conflict of Interest

The authors declare no conflict of interest.

Author Contributions

F.S. and G.G. contributed equally to this work. G.G. and F.S. conceived the idea and prepared the samples; G.G. performed the mechanical, SEM, and actuation characterizations; L.D.B., M.C., and F.S. carried out the magnetic study; G.G., F.S., and L.D.B. wrote the original draft. N.M.P., G.G., and F.S. acquired the funding and supervised the study. All the authors approved the final version of the manuscript.

Data Availability Statement

The data that support the findings of this study are available from the corresponding author upon reasonable request.

Keywords

AFM/MFM analysis, hybrid materials, magnetic microtubes, magnetic properties, mechanical properties, sensor applications, SQUID magnetometry

Received: June 28, 2022
Revised: August 7, 2022
Published online:

[1] J. A. Rogers, T. Someya, Y. Huang, *Science* **2010**, *327*, 1603.
[2] J. Li, A. Wang, J. Qin, H. Zhang, Z. Ma, G. Zhang, *Compos. Part A Appl. Sci. Manuf.* **2021**, *140*, 106144.
[3] U. G. K. Wegst, H. Bai, E. Saiz, A. P. Tomsia, R. O. Ritchie, *Nat. Mater.* **2015**, *14*, 23.
[4] F. G. Barth, J. A. C. Humphrey, M. V. Srinivasan, *Frontiers in Sensing: From Biology to Engineering*, Springer, New York, **2013**.
[5] H. Joodaki, M. B. Panzer, *Proc. Inst. Mech. Eng., Part H* **2018**, *232*, 323.
[6] S. Bauer, *Nat. Mater.* **2013**, *12*, 871.
[7] W. Gao, H. Ota, D. Kiriya, K. Takei, A. Javey, *Acc. Chem. Res.* **2019**, *52*, 523.
[8] S. Huang, Y. Liu, Y. Zhao, Z. Ren, C. F. Guo, *Adv. Funct. Mater.* **2019**, *29*, 1805924.
[9] B. D. Gates, *Science* **2009**, *323*, 1566.
[10] M. Stoppa, A. Chiolerio, *Sensors* **2014**, *14*, 11957.
[11] D. Archilla, A. Moya, A. Hernando, P. Marín, *J. Magn. Magn. Mater.* **2019**, *469*, 289.

[12] J. Xiong, J. Chen, P. S. Lee, *Adv. Mater.* **2021**, *33*, 2002640.
[13] Y. Zhou, W. Zhu, L. Zhang, J. Gong, D. Zhao, M. Liu, L. Lin, Q. Meng, R. Thompson, Y. Sun, *J. Eng. Fiber. Fabr.* **2019**, *14*, 1.
[14] F. H. Zhang, Z. C. Zhang, C. J. Luo, I. T. Lin, Y. Liu, J. Leng, S. K. Smoukov, *J. Mater. Chem. C* **2015**, *3*, 11290.
[15] G. H. Altman, F. Diaz, C. Jakuba, T. Calabro, R. L. Horan, J. Chen, H. Lu, J. Richmond, D. L. Kaplan, *Biomaterials* **2003**, *24*, 401.
[16] D. U. Shah, D. Porter, F. Vollrath, *Compos. Sci. Technol.* **2014**, *101*, 173.
[17] Y. Zhang, C. Chen, Y. Qiu, L. Ma, W. Qiu, R. Yu, W. Yu, X. Y. Liu, *Adv. Funct. Mater.* **2021**, *31*, 2100150.
[18] Z. Jia, J. Gong, Y. Zeng, J. Ran, J. Liu, K. Wang, C. Xie, X. Lu, J. Wang, *Adv. Funct. Mater.* **2021**, *31*, 2010461.
[19] Q. Niu, X. Huang, S. Lv, X. Yao, S. Fan, *J. Mater. Chem. A* **2020**.
[20] C. Holland, K. Numata, J. Rnjak-Kovacina, F. P. Seib, *Adv. Healthcare Mater.* **2019**, 8.
[21] G. Greco, V. Mastellari, C. Holland, N. M. Pugno, *Perspect. Sci.* **2021**, *29*, 133.
[22] G. Greco, N. M. Pugno, *Molecules* **2020**, 25.
[23] I. Agnarsson, M. Kuntner, T. A. Blackledge, *PLoS One* **2010**, *5*, e11234.
[24] C. Allmeling, A. Jokuszies, K. Reimers, S. Kall, C. Y. Choi, G. Brandes, C. Kasper, T. Scheper, M. Guggenheim, P. M. Vogt, *Cell Prolif* **2008**, *41*, 408.
[25] T. Kornfeld, J. Nessler, C. Helmer, R. Hannemann, K. H. Waldmann, C. T. Peck, P. Hoffmann, G. Brandes, P. M. Vogt, C. Radtke, *Biomaterials* **2021**, *271*, 120692.
[26] A. Dellaquila, G. Greco, E. Campodoni, M. Mazzocchi, B. Mazzolai, A. Tampieri, N. M. Pugno, M. Sandri, *J. Appl. Polym. Sci.* **2020**, *137*, 48739.
[27] E. L. Mayes, F. Vollrath, S. Mann, *Adv. Mater.* **1998**, *10*, 801.
[28] Z. Shao, F. Vollrath, *Polymer* **1999**, *40*, 1799.
[29] G. Greco, T. Arndt, B. Schmuck, J. Francis, F. G. Bäcklund, O. Shilkova, A. Barth, N. Gonska, G. Seisenbaeva, V. Kessler, J. Johansson, N. M. Pugno, A. Rising, *Commun. Mater.* **2021**, *2*, 43.
[30] M. Elices, G. R. Plaza, J. Pérez-Rigueiro, G. V. Guinea, *J. Mech. Behav. Biomed. Mater.* **2011**, *4*, 658.
[31] S. M. Lee, E. Pippel, U. Gösele, C. Dresbach, Y. Qin, C. V. Chandran, T. Bräuniger, G. Hause, M. Knez, *Science* **2009**, *324*, 488.
[32] P. Morales, B. Rapone, M. Caruso, D. Flammini, *Nanotechnology* **2012**, 23.
[33] X. Li, L. Zong, X. Wu, J. You, M. Li, C. Li, *J. Mater. Chem. C* **2018**, *6*, 3212.
[34] E. Steven, W. R. Saleh, V. Lebedev, S. F. A. Acquah, V. Laukhin, R. G. Alamo, J. S. Brooks, *Nat. Commun.* **2013**, *4*, 2435.
[35] L. Pan, F. Wang, Y. Cheng, W. R. Leow, Y. W. Zhang, M. Wang, P. Cai, B. Ji, D. Li, X. Chen, *Nat. Commun.* **2020**, 11.
[36] D. W. Choi, K. L. Choy, *Mater. Des.* **2020**, *191*, 108669.
[37] N. Singh, D. Mondal, M. Sharma, R. V. Devkar, S. Dubey, K. Prasad, *ACS Sustainable Chem. Eng.* **2015**, *3*, 2575.
[38] T. A. Blackledge, J. E. Swindeman, C. Y. Hayashi, *J. Exp. Biol.* **2005**, *208*, 1937.
[39] G. Greco, H. Mirbaha, B. Schmuck, A. Rising, N. M. Pugno, *Sci. Rep.* **2022**, *12*, 3507.
[40] G. Greco, M. F. Pantano, B. Mazzolai, N. M. Pugno, *Sci. Rep.* **2019**, *9*, 5776.
[41] G. Greco, J. O. Wolff, N. M. Pugno, *Front. Mater.* **2020**, 7.
[42] F. G. Bäcklund, B. Schmuck, G. H. B. Miranda, G. Greco, N. M. Pugno, J. Rydén, A. Rising, *Materials* **2022**, *15*, 708.
[43] H. Peterlik, *J. Mater. Sci.* **1995**, *30*, 1972.
[44] R. S. Sundar, S. C. Deevi, *Int. Mater. Rev.* **2005**, *50*, 157.
[45] J. H. Thomas, *J. Vac. Sci. Technol. A Vacuum, Surfaces, Film.* **2003**, *21*, 572.
[46] S. Merabtine, F. Zighem, D. Faurie, A. Garcia-Sanchez, P. Lupo, A. O. Adeyeye, *Nano Lett.* **2018**, *18*, 3199.
[47] D. Faurie, F. Zighem, A. Garcia-Sanchez, P. Lupo, A. O. Adeyeye, *Appl. Phys. Lett.* **2017**, *110*, 091904.
[48] S. Merabtine, F. Zighem, A. Garcia-Sanchez, V. Gunasekaran, M. Belmeguenai, X. Zhou, P. Lupo, A. O. Adeyeye, D. Faurie, *Sci. Rep.* **2018**, *8*, 13695.
[49] P. Echlin, *Handbook of Sample Preparation for Scanning Electron Microscopy and X-Ray Microanalysis*, Springer US, Boston, MA, **2009**.
[50] T. A. Blackledge, R. A. Cardullo, C. Y. Hayashi, *Invertebr. Biol.* **2005**, *124*, 165.
[51] K. Wasa, I. Kanno, H. Kotera, *Handbook of Sputter Deposition Technology: Fundamentals and Applications for Functional Thin Films, Nano-Materials and MEMS*, 2nd ed., Elsevier, Amsterdam **2012**.
[52] X. Liu, H. Kanda, A. Morisako, *J. Phys. Conf. Ser.* **2011**, *266*, 012037.
[53] M. Mirigliano, S. Radice, A. Falqui, A. Casu, F. Cavaliere, P. Milani, *Sci. Rep.* **2020**, *10*, 19613.
[54] K. H. Mller, M. M. A. Yajadda, *J. Appl. Phys.* **2012**, *111*, 123705.
[55] O. Glushko, M. J. Cordill, *Exp. Tech.* **2016**, *40*, 303.
[56] N. Challab, A. D. Aboumassound, F. Zighem, D. Faurie, M. Haboussi, *J. Phys. D. Appl. Phys.* **2019**, *52*, 355004.
[57] S. Merabtine, F. Zighem, D. Faurie, A. Garcia-Sanchez, P. Lupo, A. O. Adeyeye, *Nano Lett.* **2018**, *18*, 3199.
[58] M. J. Cordill, F. D. Fischer, F. G. Rammerstorfer, G. Dehm, *Acta Mater.* **2010**, *58*, 5520.
[59] Y. Kudriavtsev, A. Villegas, A. Godines, R. Asomoza, *Appl. Surf. Sci.* **2005**, *239*, 273.
[60] D. Depla, W. P. Leroy, *Thin Solid Films* **2012**, *520*, 6337.
[61] R. Ene, C. Krywka, S. G. Kang, P. Papadopoulos, M. Burghammer, E. Di Cola, M. Müller, F. Kremer, *Polymer* **2012**, *53*, 5507.
[62] G. Zandomeneghi, M. R. H. Krebs, M. G. McCammon, M. Fändrich, *Protein Sci.* **2009**, *13*, 3314.
[63] G. Greco, J. Francis, T. Arndt, B. Schmuck, F. G. Bäcklund, A. Barth, J. Johansson, N. M. Pugno, A. Rising, *Molecules* **2020**, 25.
[64] S. Inamdar, M. Ramudu, M. M. Raja, S. V. Kamat, *J. Magn. Magn. Mater.* **2016**, *418*, 175.
[65] F. Chinni, F. Spizzo, F. Montoncello, V. Mattarello, C. Maurizio, G. Mattei, L. Del Bianco, *Materials (Basel)*. **2017**, *10*, 717.
[66] M. P. Proenca, C. T. Sousa, J. Ventura, J. P. Araújo, in *Magnetic Nano- and Microwires: Design, Synthesis, Properties and Applications*, (Ed: M. Vázquez), Elsevier, Amsterdam **2015**, p. 727.
[67] M. Staňo, O. Fruchart, in *Handbook of Magnetic Materials*, (Ed: E. Brück), Elsevier, Amsterdam, Netherlands **2018**, p. 155.
[68] X. F. Han, S. Shamaila, R. Sharif, J. Y. Chen, H. R. Liu, D. P. Liu, *Adv. Mater.* **2009**, *21*, 4619.
[69] K. Yazawa, A. D. Malay, H. Masunaga, Y. Norma-Rashid, K. Numata, *Commun. Mater.* **2020**, *1*, 10.
[70] A. Vansteenkiste, J. Leliaert, M. Dvornik, M. Helsen, F. Garcia-Sanchez, B. Van Waeyenberge, *AIP Adv.* **2014**, *4*, 107133.
[71] J. Leliaert, B. Van de Wiele, A. Vansteenkiste, L. Laurson, G. Durin, L. Dupré, B. Van Waeyenberge, *J. Appl. Phys.* **2014**, *115*, 233903.
[72] L. Exl, S. Bance, F. Reichel, T. Schrefl, H. Peter Stimming, N. J. Mauser, *J. Appl. Phys.* **2014**, *115*, 17D118.
[73] H. T. Tran, T. Do, W. Cai, *Thin Solid Films* **2019**, *689*, 137493.
[74] S. Baco, Q. A. Abbas, T. J. Hayward, N. A. Morley, *J. Alloys Compd.* **2021**, *881*, 160549.
[75] K. S. Chan, H. Ji, X. Wang, S. J. Hudak, B. R. Lanning, *Mater. Sci. Eng. A* **2006**, *422*, 298.
[76] P. R. Buckley, G. H. McKinley, T. S. Wilson, W. SmallIV, W. J. Benett, J. P. Bearinger, M. W. McElfresh, D. J. Maitland, *IEEE Trans. Biomed. Eng.* **2006**, *53*, 2075.
[77] G. Katarivas Levy, M. A. Birch, R. A. Brooks, S. Neelakantan, A. E. Markaki, *J. Clin. Med.* **2019**, *8*, 1522.
[78] E. B. Joyee, Y. Pan, *Soft Robot* **2019**, *6*, 333.

[79] L. Gao, J. Wang, S. Guan, M. Du, K. Wu, K. Xu, L. Zou, H. Tian, Y. Fang, *Nano Lett.* **2019**, *19*, 8032.
[80] A. Mukherjee, S. Sudersan, S. F. Ali, A. Arockiarajan, *Smart Mater. Struct.* **2021**, 30.
[81] B. Schmuck, G. Greco, A. Barth, N. M. Pugno, J. Johansson, A. Rising, *Mater. Today* **2021**, *50*, 16.
[82] F. Spizzo, M. Tamisari, F. Chinni, E. Bonfiglioli, L. Del Bianco, *J. Magn. Magn. Mater.* **2017**, *421*, 234.
[83] T. K. Maugel, J. I. Goldstein, H. Yakowitz, *Trans. Am. Microsc. Soc.* **1976**, *95*, 242.
[84] H. N. Southworth, in *Physicochemical Methods of Mineral Analysis* (Ed: A. W. Nicole). Springer, Boston, MA, **1975**.
[85] C. A. Schneider, W. S. Rasband, K. W. Eliceiri, *Nat. Methods* **2012**, *9*, 671.
[86] F. Spizzo, E. Bonfiglioli, M. Tamisari, A. Gerardino, G. Barucca, A. Notargiacomo, F. Chinni, L. Del Bianco, *Phys. Rev. B* **2015**, *91*, 064410.
[87] M. Grimsditch, P. Vavassori, *J. Phys. Condens. Matter* **2004**, *16*, R275.
[88] J. M. D. Coey, *Magnetism and Magnetic Materials*, Cambridge University Press, New York, **2010**.